

REPORT

THERMAL CONDUCTIVITY

Experimental observation of high thermal conductivity in boron arsenide

Joon Sang Kang, Man Li, Huan Wu, Huuduy Nguyen, Yongjie Hu*

Improving the thermal management of small-scale devices requires developing materials with high thermal conductivities. The semiconductor boron arsenide (BAs) is an attractive target because of ab initio calculation indicating that single crystals have an ultrahigh thermal conductivity. We synthesized BAs single crystals without detectable defects and measured a room-temperature thermal conductivity of 1300 watts per meter-kelvin. Our spectroscopy study, in conjunction with atomistic theory, reveals that the distinctive band structure of BAs allows for very long phonon mean free paths and strong high-order anharmonicity through the four-phonon process. The single-crystal BAs has better thermal conductivity than other metals and semiconductors. Our study establishes BAs as a benchmark material for thermal management applications and exemplifies the power of combining experiments and ab initio theory in new materials discovery.

The decreasing size of modern electronics makes heat dissipation one of the most critical technological challenges. The worldwide semiconductor industry, which has powered the information technology revolution since the 1960s, acknowledged in 2016 that Moore's law is nearing its end (1). A major issue is the enormous amount of waste heat generated during electronic device operation (2, 3). For example, a U.S. data center devotes about 50% of its total electricity use to cooling (4). At the nanoscale, the power density of hot spots in current transistors is approaching that of the Sun's surface (5). Low thermal conductivity and heat dissipation rates severely degrade the performance and energy efficiency of electronic and photonic devices. Thermal management is arguably the biggest roadblock for next-generation devices, such as microprocessors and integrated circuits, light-emitting diodes, and high-power radio frequency devices, to name just a few (1, 5).

Discovering high thermal conductivity (HTC) materials is needed to enable efficient heat dissipation from hot spots and improve device performance. So far, much of the research has been focused on carbon-based crystals—diamond, graphene, and carbon nanotubes. Although these materials can have exceptional heat transfer properties, there are several drawbacks for widespread use. Diamond, the most developed material for passive cooling of high-power electronics, suffers from high cost, slow synthesis rates, low quality, and challenging integration with semiconductors. Degradation of thermal conductivity plagues graphene and nanotubes when

assembled into practical sizes, owing to ambient interactions and disorder scattering. Their intrinsic anisotropy creates other challenges for applications.

Fundamentally, understanding the origins of HTC remains a challenge. The conventionally accepted criteria for HTC materials are (i) small average atomic mass (\bar{M}); (ii) strong interatomic bonding; (iii) simple crystal structure; and (iv) low anharmonicity (6–8). Criteria (i) and (ii) imply a large Debye temperature (Θ_D) and provide the commonly used rule of thumb that thermal conductivity increases with decreasing \bar{M} and increasing Θ_D . Diamond is the prototypical crystal. Diamond's two-atom primitive unit cell, light carbon mass, and stiff covalent bonding result in an exceptionally high value for thermal conductivity. Recent ab initio calculations show excellent agreement with the measured thermal conductivity of a wide range of materials (8–16), including silicon, diamond, graphene, and carbon nanotubes. Such calculations provide new physical insights into the nature of phonon thermal transport and the HTC mechanism.

Recent ab initio theoretical work indicates that the conventional criteria for HTC materials are incomplete and points to new ones stemming from fundamental vibrational properties that can lead to HTC (8, 16–18). These new criteria applied to binary compounds are (i) a large mass ratio of constituent atoms; (ii) bunching together of the acoustic phonon branches; and (iii) an isotopically pure heavy atom. The large mass ratio provides a large frequency gap between acoustic and optical phonons (a-o gap). According to materials examined thus far, bunching of the acoustic phonon dispersions tends to occur in crystals with light constituent atoms, such as boron and carbon, where it derives from an unusual interatomic bonding that lacks core p electrons (19).

Criteria (i) and (ii) contribute to unusually weak phonon-phonon scattering (20) and a large intrinsic thermal conductivity, whereas criteria (i) and (iii) cause relatively weak scattering of phonons by isotopes (21, 22). The ab initio theory identified the III-V zinc-blende compound, defect-free boron arsenide (BAs), as having an exceptionally high thermal conductivity of more than 1000 W/m-K (8, 16–18). This predicted HTC exceeds that of most state-of-the-art HTC materials and more than triples that of the current industrial HTC standard, i.e., silicon carbide. BAs possesses an advantageous combination of properties that incorporates both conventional (light boron mass and stiff, almost pure, covalent bonding) and new criteria [large arsenic-to-boron mass ratio, bunching together of its acoustic phonon branches, and isotopically pure As (heavy) atom] (8, 16–18).

Experimental efforts to synthesize and characterize BAs have been scarce (17). Although the growth of cubic BAs was reported in the 1950s, its detailed structural characterization and properties were not reported (23–28). Generally, boron-related materials are notably difficult to obtain in dense bulk form (29). The synthesis of BAs is further complicated by the high volatility of arsenic and the introduced vacancy defects, as well as the possible formation of subphases (e.g., $B_{12}As_2$). In a collaborative effort, we reported the earliest thermal measurements on cubic BAs using the time-domain thermoreflectance technique (30). Our thermal conductivity value of 190 W/m-K measured in BAs samples with a high density of defects is far below the theoretical expectation. Later study made improvement, but the samples still show defects and grain boundaries that degraded the crystal quality and thermal properties (31). On the basis of subsequent analysis and calculation, defect scattering plays a dominant role in those samples, which makes probing the actual intrinsic thermal conductivity of BAs impossible in the absence of high-quality BAs crystals (32).

Here, we synthesized high-quality single-crystal BAs and measured an ultrahigh thermal conductivity of 1300 W/m-K in our BAs crystals. This value exceeds that of most HTC materials and is consistent with the ab initio prediction (8, 16–18). We characterized our samples with scanning electron microscopy, Raman spectroscopy, powder x-ray diffraction (P-XRD), single-crystal x-ray diffraction (S-XRD), and high-resolution transmission electron microscopy (HRTEM). BAs has a zinc-blende face-centered cubic (fcc) crystal structure in the $F\bar{4}3m$ space group, where boron and arsenic atoms are interpenetrating and covalently bonded to form a tetrahedral geometry (Fig. 1A). The Raman spectroscopy data (Fig. 1C) clearly show two peaks, at 700 and 720 cm^{-1} , corresponding to the separate vibrational behaviors of two boron isotopes (^{10}B and ^{11}B) in their natural abundance, respectively. The P-XRD peaks that we observed (Fig. 1D) are in agreement with the zinc-blende fcc crystal structure. Our S-XRD confirmed the $F\bar{4}3m$ space group and the crystal quality, and was performed to unambiguously verify the single domain, single-crystalline

School of Engineering and Applied Science, University of California, Los Angeles (UCLA), Los Angeles, CA 90095, USA.
*Corresponding author. Email: yhu@seas.ucla.edu

nature over entire crystals (33). Each of the reflections in the x-ray diffraction pattern (Fig. 1E) appears clearly as a single dot without distortion, indicating that the sample has no grain boundaries. To collect a complete dataset of all reciprocal lattice points through the whole crystal, we rotated BAS samples over 360° under x-ray excitation and collected diffraction data at every 0.3° rotation. The reconstructed reciprocal lattice images from the S-XRD [see [100] plane in Fig. 1F and (34)] confirms the single-domain, single-crystalline zinc-blende fcc structure with a cubic lattice constant of 4.78 Å over the entire BAS sample. We used a focused ion beam to thin samples to ~100 nm for HRTEM (Fig. 1G). HRTEM images (Fig. 1H) clearly demonstrate the atomically resolved single-crystal lattice of our BAS sample. The reciprocal lattice peaks obtained from two-dimensional Fourier transforms of the lattice-resolved image (inset to Fig. 1H) were indexed in the zinc-blende structure with the zone axes along the [111] direction. The measured distance between each fringe is 1.69 Å, which is consistent with (202) lattice spacing of BAS crystals (23) given the diffraction selection rules (35).

We characterized the thermal properties and phonon transport using ultrafast optical pump-probe spectroscopy based on the time-domain thermoreflectance (TDTR) technique (15, 30, 36). TDTR is well suited for the study as no physical contact is required with the sample and the measurement can provide high spatial resolution at the micrometer scale. We exposed our sample to a train of short pulses from a pump

laser that creates a temperature rise at the sample surface (Fig. 2A). The transient temperature decay, caused by the heat impulse, was monitored with another probe pulse that is delayed in time with respect to the pump using a mechanical delay stage. The thermal conductivity was obtained by fitting the full transient decay curve, acquired by varying the time delay, to a thermal model (Fig. 2B). We measured a room-temperature thermal conductivity of our high-quality BAS crystals of ~1300 W/m·K. This value exceeds that of any known metal and semiconductor and is more than three times as high as that of industrial standards (copper and silicon carbide).

We simultaneously performed TDTR measurements on single-crystal BAS, diamond, and cubic boron nitride (BN) samples to ensure accuracy and provide direct comparison between the materials (34). We measured the temperature-dependent thermal conductivity of these samples from 300 to 600 K (Fig. 2C). Our thermal conductivity values for diamond (from 2200 to 1050 W/m·K for the temperature range) are consistent with values from the literature (37–39) and validate our approach. All samples had decreased thermal conductivities with increased temperature, indicating Umklapp scattering due to increasing phonon population. This also indicates a high single-crystal quality as phonon-defect scattering behavior is not observed. The thermal conductivity of BAS is almost twice that of cubic BN, making BAS the second-highest thermally conducting material among all known isotropic

materials, exceeded only by diamond. As a semiconductor, BAS has a high potential for manufacturing integration and holds promise for thermal management applications.

Fundamentally, thermal transport in solids can be described by the interactions of phonons, i.e., the quantum-mechanical modes of lattice vibrations (6). Thermal conductivity results from phonon scattering processes that are closely related to the structure of materials. Phonon scattering usually includes Umklapp phonon-phonon scattering (τ_U), phonon-electron scattering (τ_{ph-e}), mass fluctuation scattering (τ_M), and boundary scattering (τ_B) that can be characterized by the following relaxation rate $1/\tau$ (τ is the corresponding relaxation time):

$$\frac{1}{\tau} = \frac{1}{\tau_U} + \frac{1}{\tau_{ph-e}} + \frac{1}{\tau_M} + \frac{1}{\tau_B} \quad (1)$$

Previous research indicates that the last two terms of this equation— τ_M and τ_B —play important roles in the thermal conductivity of crystals with defects and grain boundaries (32). τ_{ph-e} is non-negligible for doped semiconductors, or metals with sufficiently high electron density. Notably, the first term of the equation— τ_U —describes the thermal conductivity of perfect single crystals without any defects, and therefore is expected to be the dominant transport mechanism in our high-quality BAS single crystals. However, a persistent fundamental question regarding the high-order phonon anharmonicity, in particular for BAS, remains in the field of atomistic phonon theory. For many decades, thermal transport in solids

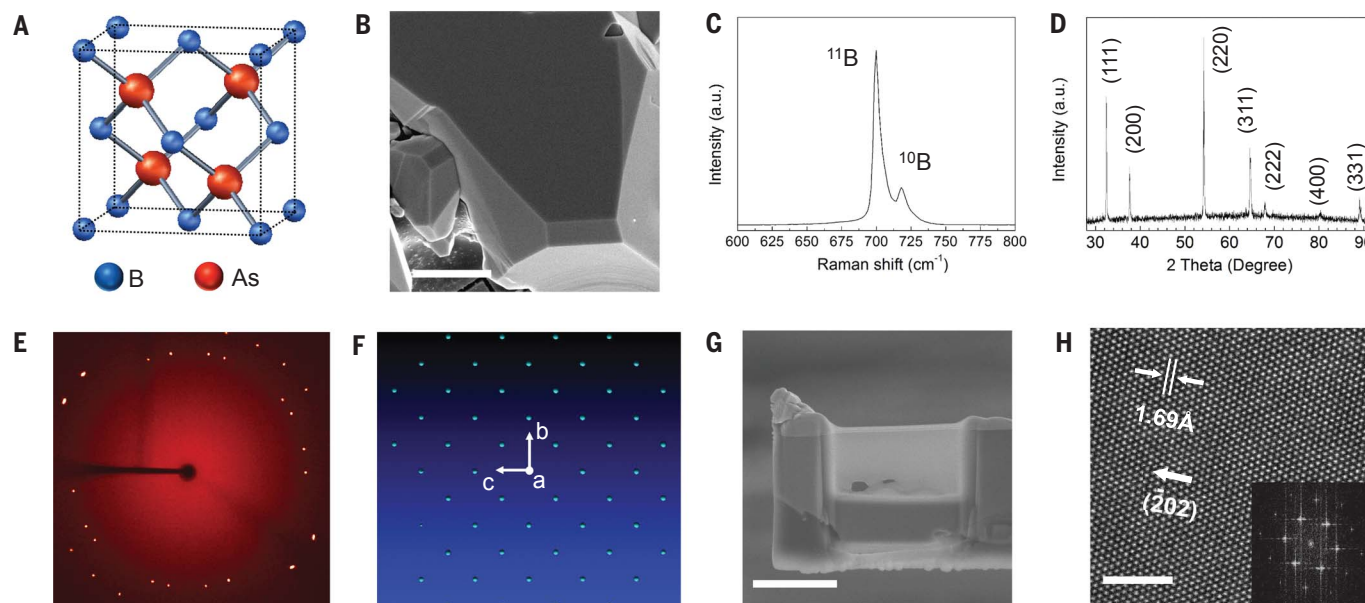


Fig. 1. Structural characterizations of single-crystal BAS. (A) Schematic of the zinc-blende crystal structure of cubic BAS, resembling that of diamond. (B) Scanning electron microscope (SEM) image of BAS. Scale bar: 5 μm. (C) Raman spectra of BAS crystals. (D) Powder x-ray diffraction measurements. (E) Single-crystal x-ray diffraction image of BAS. (F) Constructed reciprocal lattice of BAS from the complete dataset of single-crystal x-ray diffraction measurements, representing a clear

single-crystal reciprocal space over the entire crystal. The lattice constant was measured as 4.78 Å for cubic BAS. (G) SEM image of a BAS sample thin slice (~100 nm) prepared by focused ion beam for HRTEM studies. Scale bar: 3 μm. (H) HRTEM image of BAS showing atomically resolved lattices. Inset: Two-dimensional Fourier transforms of the image depicting the [111] zone axes of BAS; the arrow indicates the crystal direction of (202). Scale bar: 2 nm.

was considered to be governed by the three-phonon scattering process (6, 40), and the effects of four-phonon and higher-order scattering processes were believed to be negligible. The three-phonon scattering was deployed in the initial ab initio calculations of the BAs thermal conductivity (8), but according to recent theory (16, 41), the four-phonon scattering is important in certain materials such as BAs. The two density functional theory (DFT)-based calculations predict different thermal conductivity values for BAs. We compared our experimental measurements at different temperatures with two DFT theory predictions (Fig. 2D). In addition, to compare and exclude the effect of point defects, we performed three-phonon DFT calculation with vacancies (34) and included it in the figure. We found that our experimental results are in good agreement with the four-phonon DFT calculation, verifying that the Umklapp phonon scattering dominates phonon interactions. Moreover, our experiments indicate that, unlike in most materials, the probability of higher-order phonon scattering in BAs is important and cannot be ignored even around room temperature. The high-order anharmonicity that we observed for BAs is due to its distinctive band structure (i.e., large a-o gap and large mass ratio) that leads to a relatively weak three-phonon process and provides sufficient numbers of possible four-phonon scattering configurations.

Another important phonon mechanism for HTC in BAs is the unique phonon mean free path (MFP) spectra that come from its extraordinary phonon band structure. MFPs represent the characteristic lengths corresponding to the distance over which heat carriers transmit thermal energy before being scattered; in general, MFPs can span several orders of magnitude—usually from

~1 nm to ~100 μm . According to the ab initio theory, BAs has a large phononic band gap between acoustic and optical phonon branches, which minimizes acoustic-optical phonon scattering and leads to MFPs longer than those of most common materials. In particular, BAs phonons with MFPs longer than 1 μm contribute to more than 90% of its total thermal conductivity (18). By comparison, for diamond and cubic BN, phonons with MFPs longer than 1 μm only contribute to about 30% of their total thermal conductivity. To gain further insight and verify the phonon MFP distribution in BAs, we probed the phonon spectral contribution by exploiting the size-dependent ballistic transport (15). In essence, thermal conductivity represents the spectral contribution from many different phonon modes and can be quantified using the cumulative thermal conductivity (42) expressed as

$$\kappa(\Lambda_m) = - \int_0^{\Lambda_m} \frac{1}{3} C \cdot v \cdot \Lambda \left(\frac{d\Lambda}{d\omega} \right)^{-1} d\Lambda \quad (2)$$

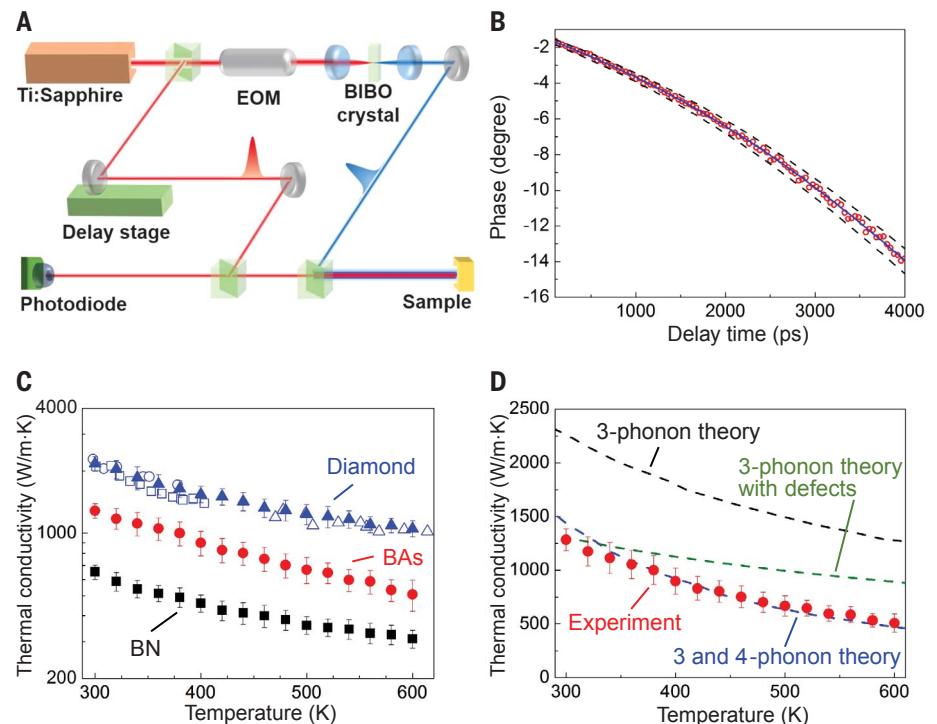
where C , v , and Λ are the phonon mode (ω)-dependent heat capacity, group velocity, and phonon MFP, respectively. The cumulative thermal conductivity— $\kappa(\Lambda_m)$ —represents the contribution to the total thermal conductivity from all phonons with MFPs shorter than a certain value, Λ_m . This quantitative spectral information projects the contributions to thermal conductivity into characteristic length scales and is key to understanding thermal properties in connection with atomistic phonon theory (42).

Experimentally, this phonon MFP distribution information can be investigated by exploiting the ballistic (or nonequilibrium) heat conduction around a small heating area, with the physical

concept described in our recently developed thermal spectral mapping spectroscopy technique (Fig. 3A) (15, 36). In this measurement, hot phonons travel from the heated area into the underlying substrate material. The heat transfer regime is controlled by a characteristic thermal length, which is proportional to the heating size D , in comparison to phonon MFPs. In the diffusive limit, when $D \gg \Lambda$, propagating phonons experience enough scattering to reach local thermal equilibrium. In this case, Fourier's law accurately describes the transport and heat flux, and the thermal conductivity of materials is simply the bulk value (κ_{bulk}). From the kinetic theory (6), the contribution to the total thermal conductivity from a specific phonon mode is $\kappa_{\omega, \text{bulk}} = \frac{1}{3} C_{\omega} \cdot v_{\omega} \cdot \Lambda_{\omega}$. As the heater size D decreases, phonons with $D < \Lambda$ will have fewer opportunities to scatter. In the ballistic limit ($D \ll \Lambda$), phonons propagate analogously to the thermal radiation over the whole region with a characteristic length of $\sim D$. Therefore, the actual heat flux will deviate from the Fourier's law prediction for the quasi-ballistic, or ballistic, regimes (Fig. 3A). Mathematically, the actual heat flux is measured and fitted to Fourier's law to obtain an effective thermal conductivity (κ_{eff}), which gradually decreases in value for smaller D s, as a higher portion of phonons evolves from diffusive to ballistic transport. The decrease in $\kappa_{\text{eff}}(D)$ represents MFP spectra and should follow the same trend in $\kappa(\Lambda_m)$. Therefore, the size-dependent thermal conductivity measurement can provide a fundamental understanding of such MFP spectra, although the exact relationship between κ_{eff} and D requires careful atomistic and multiscale simulations and is a function of the heating geometry and materials (15, 36).

Fig. 2. Temperature-dependent thermal transport measurements.

(A) Schematic of the setup for ultrafast pump-probe spectroscopy via the time-domain thermoreflectance (TDTR) technique. (B) Typical TDTR data: thermal reflectance phase signal versus time (red circles), fitted to the thermal transport model (blue line). Calculated curves (black dashed lines) with the thermal conductivity changed by $\pm 10\%$ of the best values to illustrate measurement accuracy. (C) Temperature-dependent (300 to 600 K) thermal conductivity of the three materials with the highest thermal conductivities: diamond, BAs, and boron nitride (BN). Black squares, red circles and blue triangles indicate cubic BN, BAs, and diamond, respectively. Also shown are literature data for diamond [open blue circles (38), squares (37), and triangles (39)]. (D) Experimentally measured thermal conductivity of BAs in comparison to ab initio predictions by DFT, considering the three-phonon scattering process (black dashed line) (8), the three- and four-phonon scattering process (blue dashed line) (16), and the three-phonon scattering process with point defects (green dashed line) (34).



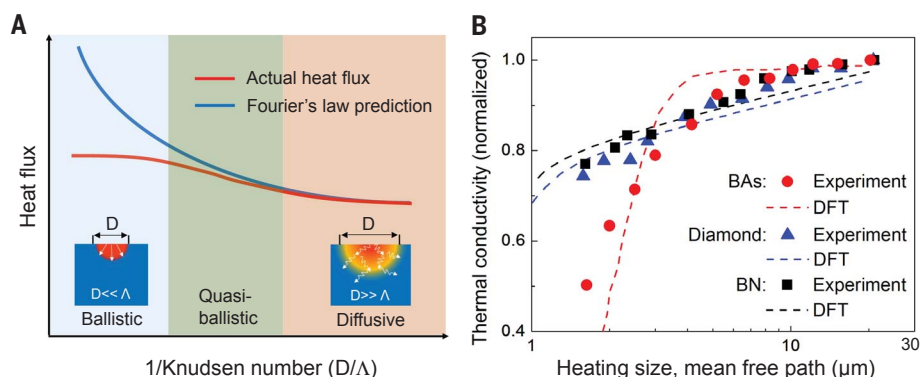


Fig. 3. Probing phonon mean free path spectra of BAs through size-dependent ballistic transport. (A) Schematic of heat flux for a fixed temperature difference as a function of the Knudsen number. Red and blue lines indicate the actual heat flux and the flux predicted by Fourier's law, respectively. Insets show that the thermal transport evolves from a diffusive to a ballistic regime when the heating size is gradually reduced. When the actual heat flux was measured and fitted to Fourier's law to obtain an effective thermal conductivity (κ_{eff}), a gradual reduction in κ_{eff} was expected with a decreasing heating size. Essentially, the κ_{eff} decrease is due to the evolution from diffusive to ballistic transport for the phonons with a mean free path comparable to the heating size, and thereby represents the phonon MFP spectra. (B) The normalized effective thermal conductivity was measured for the three best thermal conductors (BAs, diamond, and BN), as a function of heating diameters from 21 to 1.6 μm . Experimental results, compared with the MFP spectra calculated with DFT (8, 16, 18), indicate that in BAs, a large portion of phonons have long mean free paths, owing to the distinctive band structure of BAs.

In our experiments, the laser beam served as the heater, and we measured the effective thermal conductivity of materials by varying the laser heating size from 21 to 1.6 μm . The thermal conductivity of BAs, diamond, and cubic BN were measured simultaneously as a function of the heating sizes (Fig. 3B). The results clearly show that ballistic transport occurs in all three materials, but that their thermal conductivity decreases differ. For diamond and cubic BN, κ_{eff} decreases by ~ 26 and 23%, respectively, when reducing the laser heating size from 21 to 1.6 μm . By comparison, under the same conditions, a strong thermal conductivity reduction of $\sim 50\%$ is observed for BAs, indicating that long MFP phonons contribute substantially more to heat conduction in BAs crystals. Our measurements (Fig. 3B) are consistent with the DFT-predicted results for these materials (8, 16, 18). Phonons with long phonon MFPs (1 to 10 μm) contribute to a very high portion of BAs's total thermal conductivity ($>50\%$). By comparison, in most known materials, phonon MFPs are distributed over a wider range (1 nm to 100 μm). Thus, we demonstrated that the ultrahigh thermal conductivity of BAs originates from the enhanced MFPs resulting from its distinctive phonon band structure.

We experimentally observed an ultrahigh thermal conductivity of 1300 W/m \cdot K at room temperature in synthetic high-quality single-crystal BAs. Our study verifies the prediction from ab initio theory and establishes BAs as a benchmark material with the highest isotropic thermal conductivity of bulk metals and semiconductors. Our temperature-dependent data suggest that, unlike most common materials, high-order phonon an-

harmonicity strongly affects heat conduction in BAs. Furthermore, the phonon spectral contribution to thermal conductivity, investigated by exploiting the ballistic thermal transport, shows that compared to most materials, in BAs long phonon MFPs contribute to a substantially higher portion of the thermal conductivity. The investigation of fundamental transport mechanisms represents an important breakthrough in advancing the experiment-theory synergy for the rational design of new materials. Looking to the future, the ultrahigh thermal conductivity of BAs, together with its semiconducting nature and manufacturing integration, could revolutionize the current technological paradigms of thermal management and possibly extend the roadmap for high-power electronics.

REFERENCES AND NOTES

- M. M. Waldrop, *Nature* **530**, 144–147 (2016).
- P. Ball, *Nature* **492**, 174–176 (2012).
- S. Chu, A. Majumdar, *Nature* **488**, 294–303 (2012).
- W. L. Arman Shehabi, Sarah Smith, Dale Sartor, Richard Brown, Magnus Herrlin, Jonathan Koomey, Eric Masanet, Nathaniel Horner, Inês Azevedo, United States Data Center Energy Usage Report (2016); <https://ses.lbl.gov/publications/united-states-data-center-energy>.
- International Technology Roadmap for Semiconductors, ITRS 2.0 2015 Edition; www.itrs2.net/.
- J. M. Ziman, *Electrons and Phonons: The Theory of Transport Phenomena in Solids*. Oxford Classic Texts in the Physical Sciences (Oxford Univ. Press, 1960).
- G. A. Slack, *J. Phys. Chem. Solids* **34**, 321–335 (1973).
- L. Lindsay, D. A. Broido, T. L. Reinecke, *Phys. Rev. Lett.* **111**, 025901 (2013).
- N. Mingo, D. A. Broido, *Phys. Rev. Lett.* **93**, 246106 (2004).
- N. Mingo, D. A. Broido, *Phys. Rev. Lett.* **95**, 096105 (2005).
- A. Ward, D. A. Broido, D. A. Stewart, G. Deinzer, *Phys. Rev. B* **80**, 125203 (2009).

- K. Esfarjani, G. Chen, H. T. Stokes, *Phys. Rev. B* **84**, 85204 (2011).
- L. Lindsay, D. A. Broido, T. L. Reinecke, *Phys. Rev. Lett.* **109**, 095901 (2012).
- M. N. Luckyanova et al., *Science* **338**, 936–939 (2012).
- Y. Hu, L. Zeng, A. J. Minnich, M. S. Dresselhaus, G. Chen, *Nat. Nanotechnol.* **10**, 701–706 (2015).
- T. Feng, L. Lindsay, X. Ruan, *Phys. Rev. B* **96**, 161201 (2017).
- C. Uher, *Physics (College Park Md.)* **6**, 76 (2013).
- D. A. Broido, L. Lindsay, T. L. Reinecke, *Phys. Rev. B* **88**, 214303 (2013).
- R. M. Wentzcovitch, M. L. Cohen, P. K. Lam, *Phys. Rev. B Condens. Matter* **36**, 6058–6068 (1987).
- M. Lax, P. Hu, V. Narayanamurti, *Phys. Rev. B* **23**, 3095–3097 (1981).
- L. Lindsay, D. A. Broido, T. L. Reinecke, *Phys. Rev. B* **88**, 144306 (2013).
- S. Tamura, *Phys. Rev. B* **30**, 849–854 (1984).
- J. A. Perri, S. Laplaca, B. Post, *Acta Crystallogr.* **11**, 310 (1958).
- F. V. Williams, R. A. Ruehrwein, *J. Am. Chem. Soc.* **82**, 1330–1332 (1960).
- J. Osugi, K. Shimizu, Y. Tanaka, *Proc. Jpn. Acad.* **42**, 48 (1966).
- S. M. Ku, *J. Electrochem. Soc.* **113**, 813 (1966).
- A. F. Arrington, *J. Cryst. Growth* **1**, 47–48 (1967).
- T. L. Chu, A. E. Hyslop, *J. Appl. Phys.* **43**, 276–279 (1972).
- P. Rudolph, Ed., *Handbook of Crystal Growth, Vol. II, Bulk Crystal Growth* (Elsevier, 2015); <http://store.elsevier.com/Handbook-of-Crystal-Growth/isbn-9780444633033/>.
- B. Lv et al., *Appl. Phys. Lett.* **106**, 074105 (2015).
- F. Tian et al., *Appl. Phys. Lett.* **112**, 031903 (2018).
- N. H. Protik, J. Carrete, N. A. Katcho, N. Mingo, D. Broido, *Phys. Rev. B* **94**, 045207 (2016).
- B. E. Warren, *X-ray Diffraction* (Addison-Wesley, MA, 1969).
- Materials and methods are available as supplementary materials.
- D. B. Williams, C. B. Carter, *Transmission Electron Microscopy: A Textbook for Materials Science* (Springer, Boston, MA, 2009).
- J. S. Kang, H. Wu, Y. Hu, *Nano Lett.* **17**, 7507–7514 (2017).
- D. G. Onn, A. Witek, Y. Z. Qiu, T. R. Anthony, W. F. Banholzer, *Phys. Rev. Lett.* **68**, 2806–2809 (1992).
- L. Wei, P. K. Kuo, R. L. Thomas, T. R. Anthony, W. F. Banholzer, *Phys. Rev. Lett.* **70**, 3764–3767 (1993).
- J. R. Olson et al., *Phys. Rev. B Condens. Matter* **47**, 14850–14856 (1993).
- A. Maradudin, A. Fein, *Phys. Rev.* **128**, 2589–2608 (1962).
- L. Lindsay, D. A. Broido, *J. Phys. Condens. Matter* **20**, 165209 (2008).
- F. Yang, C. Dames, *Phys. Rev. B* **87**, 035437 (2013).

ACKNOWLEDGMENTS

We thank H. Albrecht for editorial help, T. Aoki from UCI Materials Research Institute for help with TEM study, and the support from UCLA CNSI and Nanolab. **Funding:** Y.H. acknowledges support from a CAREER award from the EPM and TTP programs of the National Science Foundation under grant 1753393, a Young Investigator Award from the United States Air Force Office of Scientific Research under grant FA9550-17-1-0149, a PRF Doctoral New Investigator Award from the American Chemical Society under grant 58206-DNI5, the UCLA Sustainable LA Grand Challenge, and the Anthony and Jeanne Pritzker Family Foundation. **Author contributions:** Y.H. proposed and directed the research. Y.H. and J.S.K. designed the experiment; J.S.K., M.L., and H.N. performed the experiment; H.W. performed the ab initio calculations. All authors discussed the results and commented on the manuscript. **Competing interests:** The authors declare no competing financial interests. **Data and materials availability:** All data are available in the manuscript or the supplementary materials.

SUPPLEMENTARY MATERIALS

www.sciencemag.org/content/361/6402/575/suppl/DC1
Materials and Methods
Supplementary Text
Figs. S1 to S3
References (43–58)

12 March 2018; accepted 21 June 2018
Published online 5 July 2018
10.1126/science.aat5522



www.sciencemag.org/cgi/content/full/science.aat5522/DC1

Supplementary Materials for

Experimental observation of high thermal conductivity in boron arsenide

Joon Sang Kang, Man Li, Huan Wu, Huuduy Nguyen, Yongjie Hu*

*Corresponding author. Email: yhu@seas.ucla.edu

Published 5 July 2018 on *Science* First Release

DOI: [10.1126/science.aat5522](https://doi.org/10.1126/science.aat5522)

This PDF file includes:

Materials and Methods
Supplementary Text
Figs. S1 to S3
References

Materials and Methods

Material synthesis and sample preparation

High-quality single-crystal boron arsenide (BAs) was prepared through chemical vapor transport. To minimize defects and built-in stress introduced by lattice mismatch and thermal expansion, single-crystal cubic boron phosphide (BP) was used as the growth substrate. We previously developed high-quality single-crystal BP and the details for their synthesis and preparation are described in our recent publication (36). High-purity boron and arsenic coarse powders (99.9999% purity, from Alfa Aesar) were ground by using mortar and pestle, prior to introduction into a quartz tube at a stoichiometric ratio of 1:2. After we loaded our reaction sources, the quartz tube was evacuated and flame sealed under high vacuum (10^{-5} Torr) before placement into a customized three-zone reaction furnace with a 1083 K hot zone, 1058K center zone and a 1033K cold zone. After 5 weeks at these temperatures, the quartz tube and its content were slowly cooled down to room temperature. These reaction steps were repeated until BAs single crystals of high quality were obtained. For thermal measurements, BAs samples were loaded together with single-crystal cubic boron nitride (BN) and diamond samples (from Element Six) into a cryostat (Janis ST-100 Optical Cryostat, from 4 to 800K) with a precise proportional-integral-derivative (PID) temperature controller (Lakeshore Model 335). Simultaneous thermal conductivity measurements on the three materials with the highest thermal conductivity, i.e. BAs, diamond, and BN, were performed with the time-domain thermoreflectance (TDTR) technique (see Thermal Transport Measurements section below) to guarantee measurement accuracy for high conducting materials, and enable direct comparisons between them to understand the phonon physics. For each measurement temperature, once the set temperature was reached, an additional waiting time of over 30 minutes was added before the

actual thermal measurement was performed to ensure that the samples had reached a complete thermal equilibrium and steady temperature.

Structural Characterizations

1. X-ray diffraction (XRD) measurements

Powder XRD was conducted with a Panalytical X'Pert Pro XRD machine with a Cu K α radiation source. Samples of BAs crystals were gently separated from the growth substrate and transferred to the zero-diffraction substrate. The diffractometer was operated at 45 kV and 40 mA. After measurement, the diffraction peaks were matched with the material data directory and identified as BAs crystals.

Single-crystal XRD was performed using a Bruker SMART APEX II single-crystal XRD machine equipped with a charge-coupled device (CCD) detector. A single piece of BAs crystal (~50 μm size) was separated from the growth substrate and mounted onto the goniometer stage for measurement. First, the crystal quality was carefully examined by full-angle rotation images. The BAs sample was rotated over 360 degrees under x-ray excitation, while the diffraction data was continuously collected by the CCD detector and subsequently combined into a single plot. The combined rotation images showed that the BAs crystal sample was a single crystal in its entirety. Next, to determine the unit-cell crystal structure and examine the possibility of any crystal twinning and defects, single-crystal XRD data were collected with 0.3 degree of frame width and 60s/frame of exposure time. A Mo K α radiation source was used for data collection. Following the measurements, the Bruker APEX software was used to determine the lattice constant and crystal structure. The BAs crystal sample demonstrated a perfect zinc-blende FCC crystal structure with a lattice constant of 4.78 \AA . In combination with the measured diffraction

patterns from each frame, the reciprocal lattice space (k space) of the BAs crystal sample was constructed and plotted (Fig. S1). Fig. S1a and S1b show the measured reciprocal lattice of the BAs crystal in the (001) and (010) direction, respectively. After verification of the crystallographic direction in the reciprocal lattice, we concluded that the entire BAs crystal was a homogeneous single-crystal domain without any impurity or lattice twinning.

2. Transmission electron microscopy (TEM) measurement

TEM samples were prepared by using a focused ion beam (FIB) machine (Nova 600, FEI). First, a single piece of BAs crystal was cut by FIB into small size pieces: $8\ \mu\text{m} \times 8\ \mu\text{m} \times 2\ \mu\text{m}$ (width \times height \times thickness), and placed on top of a TEM grid (PELCO FIB Lift-Out, Ted Pella) with a nanomanipulator. The BAs crystal was further milled by FIB until the sample thickness was thin enough ($< 100\ \text{nm}$) to be traversed by the electron beam for effective TEM imaging. After FIB, we used concentrated argon ion beam (Nanomill, model 1040, Fischeone) to clean the BAs sample surface. After cleaning, we took the high angle annular dark field (HAADF) image by using aberration-corrected high-resolution scanning TEM (Grand ARM, JEOL, 300 kV). Atomic-resolution TEM images and their fast Fourier transform images were processed with the Gatan TEM software.

3. Raman spectroscopy

Raman spectra were taken with a Raman microscope (inVia, Renishaw) under laser excitation at 633 nm with a 1800 /mm grating. The laser was polarized and backscattered and the Raman microscope operated with the Leica DM2500 optical system.

Thermal Transport Measurements

TDTR is routinely used to measure the thermal conductivity of a wide range of materials (14, 15, 36, 43–45). The details of the TDTR measurements are as follows. A Ti:Sapphire oscillator (Tsunami, Spectra-Physics) generates femtosecond laser pulses (100 fs) at a repetition rate of 80.7 MHz and a central wavelength at 800 nm. The laser pulse is split into pump and probe beams. The pump beam passes through an electro-optic modulator (EOM) with a sine-wave modulation up to 20 MHz and then through a bismuth triborate (BIBO) crystal, where its frequency is doubled to a wavelength of 400 nm. The modulated pump beam heats up the sample surface, creating a sharp temperature rise. The transient temperature decay is monitored by the probe beam, which is delayed with a mechanical delay stage for a sub-picosecond resolution of the temperature decay. The thermal conductivity of a sample is extracted by measuring changes in its reflectance signal with a photodetector connected to a lock-in amplifier. The lock-in amplifier transmits in-phase (V_{in}) and out-phase (V_{out}) reflectance signals. A thin aluminum film (~100 nm) was deposited on top of the sample surface for thermal transduction. The thickness of the Al film was verified by picosecond pulse-echo measurements. Sensitivity analysis is performed to optimize the experimental conditions and ensure the measurement accuracy for high thermal conductivity materials(36). Ten experimental measurements are plotted together in Figure S3.

A description of the modeling analysis to extract thermal conductivity is provided below and can be found in details in previous publications(14, 15, 36, 43–47). For each measurement, we carefully measured the root-mean-square (RMS) diameter ($1/e^2$ diameter) of the pump and probe beams by using the beam offset method (45). The pump beam was swept by a piezo-mirror mount with a step resolution of 0.7 μ rad, which is equivalent to 2 nm. We used the in-phase

signal to fit the Gaussian distribution of the laser spot.

The measured signal from the linear time invariant system in the lock-in amplifier is expressed as:

$$Z(\omega_0) = R \sum_{N=-\infty}^{\infty} H(\omega_0 + N\omega_s) \exp(iN\omega_s \tau) \quad (\text{E1}) \quad (\text{see Ref (46)})$$

where R is the constant which includes the thermoreflectance coefficient, the electronics gain. The N , ω_0 , ω_s , and τ are the integer, modulation frequency, probe frequency, and time delay. The real part in equation E1, or the in-phase signal, $\text{Re}[Z(\omega_0)]$, is related to the temperature response from the sample at short delay times. On the other hand, the out-of-phase signal, or the imaginary part of equation E1, $\text{Im}[Z(\omega_0)]$, is proportional to the imaginary temperature oscillation.

The transient heat conduction model in cylindrical coordinates is expressed as:

$$\rho C_p \frac{\partial T}{\partial t} = \frac{\kappa}{r} \frac{\partial}{\partial r} \left(r \frac{\partial T}{\partial r} \right) + \kappa \frac{\partial^2 T}{\partial z^2} \quad (\text{E2})$$

After Hankel transform and Fourier transform, equation (E2) becomes:

$$\rho C_p i f \bar{T}(\omega) + \kappa k^2 \bar{T}(\omega) = \kappa \frac{\partial^2 \bar{T}(\omega)}{\partial z^2} \quad (\text{E3})$$

where ρ , C_p , and κ are the mass density, specific heat, and thermal conductivity, respectively.

Rearrangement of equation E3 leads to:

$$\frac{\partial^2 \bar{T}(\omega)}{\partial z^2} = \beta^2 \bar{T}(\omega) \quad (\text{E4})$$

Thus β is defined as:

$$\beta \equiv \frac{\rho C_p i \omega + \kappa k^2}{\kappa} \quad (\text{E5})$$

The thermal response of a sample in a given frequency domain is expressed as:

$$\begin{pmatrix} T_b \\ q_b \end{pmatrix} = \begin{pmatrix} \cosh(\beta d) & -\frac{1}{\kappa\beta} \sinh(\beta d) \\ -\kappa\beta \sinh(\beta d) & \cosh(\beta d) \end{pmatrix} \begin{pmatrix} T_t \\ q_t \end{pmatrix} \quad (\text{E6}) \text{ (see Ref (46))}$$

where T_b , T_t , q_b , and q_t are temperatures of bottom and top sides, heat flux of bottom and top side, and d is the layer thickness. For multi-layers:

$$\begin{pmatrix} T_b \\ q_b \end{pmatrix} = K_n K_{n-1} K_{n-2} \dots K_1 \begin{pmatrix} T_t \\ q_t \end{pmatrix} = \begin{pmatrix} a_{11} & a_{12} \\ a_{21} & a_{22} \end{pmatrix} \begin{pmatrix} T_t \\ q_t \end{pmatrix} \quad (\text{E7})$$

In the semi-infinite n-th layer:

$$T_t = -\frac{a_{22}}{a_{21}} q_t \quad (\text{E8})$$

Heat flux at the top boundary surface is expressed by the Hankel transform of the Gaussian distribution of the beam spot which is:

$$q_t = \frac{A_0}{2\pi} \exp\left(-\frac{k^2 w^2}{8}\right) \quad (\text{E9})$$

where A_0 and w are the laser power and radius of beam. By taking the inverse Hankel transform of equation (E8) with the weight average by co-axial probe beam, the frequency domain solution of H in equation E1 is expressed as:

$$H(\omega) = \frac{A}{2\pi} \int_0^\infty \frac{-a_{22}}{a_{21}} \exp\left(-\frac{k^2 (w_{pump}^2 + w_{probe}^2)}{8}\right) k dk \quad (\text{E10}) \text{ (see Ref. (46))}$$

The derivations and thermal modeling analysis can be found in more details elsewhere (7, 8).

Specific Heat Measurement

The specific heat of boron arsenide was measured using the differential scanning calorimetry (PerkinElmer DSC 8000) across the temperature range from 300K to 600 K. The two

furnaces and the StepScan mode of this machine enable the precise specific heat measurement. During each measurement, there are two crimped aluminum pans scanned across the desired temperature range, in one of which the sample was loaded while the other one was empty. The difference of heat flux through the two pans is used to calculate the thermal energy required by our boron arsenide sample to elevate its temperature. Before each measurement run, a background run was performed in advance to eliminate the measurement errors of heat flux brought by the system itself. The DSC machine was calibrated with aluminum first. We performed the temperature scanning with the heating rate of 10 K/min, temperature interval of 10 K and thermalization time of 1 min under the nitrogen purge flow rate of 20 mL/min.

For mass density, we experimentally measured the lattice constant of BAs sample to be 4.78 Å using single crystal x-ray diffraction (Figure 1f in the main text and Figure S1 in the Supplement information). Considering the crystal structure and unit cell volume so we obtained the mass density is 5.214 g/cm³.

Crystal stability of BAs

To evaluate the stabilities of BAs crystals(48), we measure the thermal conductivity of our BAs crystal after 10 month from its growth. We keep our sample in the atmosphere condition (300K, 1atm, and ~ 60% of relative humidity). We found that there is no degradation in the thermal conductivity of BAs, indicating that BAs crystal is stable in the air up to 10 month. Furthermore, we confirmed temperature stability of our BAs crystal. We heat up our crystal up to 600K in the vacuum and cooling down to room temperature. We repeat the temperature cycle twice and the measured thermal conductivity remains the same. These indicate that BAs crystal is stable under these conditions.

Ab initio Calculation to Evaluate the Effect of Point Defects

We performed ab initio calculation to consider the effect of arsenic vacancy defects at different temperatures (T), following the settings in recent literature (8, 18, 32). The nonequilibrium phonon distribution function n_λ under an applied temperature gradient can be described by the Boltzmann transport equation (BTE) as

$$\mathbf{v}_\lambda \cdot \nabla T \frac{\partial n_\lambda}{\partial T} = \left(\frac{\partial n_\lambda}{\partial t} \right)_{collisions} \quad (\text{E11})$$

where $\lambda \equiv (\mathbf{q}, p)$ labels the phonon mode with wave vector \mathbf{q} and polarization p , and \mathbf{v}_λ is the phonon group velocity. In Eq. (E11), the phonon drift due to temperature gradient on the left side is balanced by the phonon scattering on the right side. The scattering term on the right side of the equation includes intrinsic phonon-phonon scattering and phonon-isotope/defect scattering,

$$\left(\frac{\partial n_\lambda}{\partial t} \right)_{collisions} = \left(\frac{\partial n_\lambda}{\partial t} \right)_{intrinsic} + \left(\frac{\partial n_\lambda}{\partial t} \right)_{defect} \quad (\text{E12})$$

For phonon scattering due to isotopes or point defects, a perturbation to Hamiltonian due to mass disorder is considered. Using Fermi's golden rule, the phonon-isotope/defect scattering term (49) in BTE is expressed as

$$\left(\frac{\partial n_\lambda}{\partial t} \right)_{defect} = \frac{\pi}{2N} \omega_\lambda^2 \sum_{\lambda'} \delta(\omega_\lambda - \omega_{\lambda'}) \sum_b g(b) |\mathbf{e}_{\lambda'}^*(b) \cdot \mathbf{e}_\lambda(b)|^2 [n_\lambda(n_{\lambda'} + 1) - n_{\lambda'}(n_\lambda + 1)] \quad (\text{E13})$$

where ω_λ is the angular frequency of phonon mode λ , $\mathbf{e}_\lambda(b)$ is the vibrational eigenvector of the b^{th} atom in unit cell and phonon mode λ , and N is the number of unit cells in the crystal. $g(b)$ is a factor that describes the mass variance of the b^{th} atom in unit cell,

$$g(b) = \sum_i f_i(b) \left[1 - \frac{M_i(b)}{\bar{M}(b)} \right]^2 \quad (\text{E14})$$

where $f_i(b)$ and $M_i(b)$ are the fraction and the atomic mass of the i^{th} isotope of the b^{th} atom respectively, and $\bar{M}(b)$ is the average atomic mass of the element of the b^{th} atom. Arsenic

vacancies are treated as an isotope to arsenic with zero mass. In this method, the changes of interatomic potential are ignored, whose influence to lattice thermal conductivity is negligible at low vacancy concentration ($< 0.01\%$) (32). For the calculation of Figure 2d in this paper, we used a vacancy concentration $\sim 0.002\%$ to match the calculated thermal conductivity with the measured value at room temperature. The calculated curve (green dashed line, Figure 2d) represents the prediction of temperature-dependent thermal conductivity when three-phonon process and defect scattering dominate the thermal transport (i.e. four-phonon process is negligible).

According to Eq. (E13), the isotope scattering term is determined by nonequilibrium phonon distribution function n_λ . Similarly, using Fermi's golden rule, phonon-phonon intrinsic scattering term $\left(\frac{\partial n_\lambda}{\partial t}\right)_{intrinsic}$ considering three-phonon process can be expressed as a function of nonequilibrium phonon distribution function and third-order interatomic force constants(11, 50). Hence, the unknown n_λ is on both sides of the BTE. To calculate the thermal conductivity of most common materials, a single mode relaxation time approximation (RTA) is usually applied to derive the phonon lifetime time, and subsequently the thermal conductivity can be derived from kinetic theory(6). Within the single mode RTA, the phonon distribution for mode λ' in Eq. (E13) (or mode λ' and λ'' for three phonon process) follows the equilibrium Bose-Einstein distribution, and a perturbation is given to mode λ , so that one can compute the phonon lifetime for mode λ by BTE. However, the single mode RTA approximation can underestimate the thermal conductivity for high thermal conductivity materials such as graphene and diamond (11). This is due to inaccurate treats of the normal phonon-phonon scattering process and the breakdown of the local equilibrium for materials with small phonon scattering rates. Therefore, instead of RTA, we used the iterative solution of BTE (11) here to calculate the thermal

conductivity of BAs. For a small temperature gradient (∇T), the nonequilibrium phonon distribution n_λ can be linearly expanded as $n_\lambda = n_\lambda^0 + (-\partial n_\lambda^0 / \partial T) \mathbf{F}_\lambda \cdot \nabla T$, where n_λ^0 is the Bose-Einstein distribution under equilibrium state. \mathbf{F}_λ can be derived by iteratively solving the BTE. The lattice thermal conductivity tensor $\kappa^{\alpha\beta}$ can be calculated by summing over all the phonon modes in first Brillouin zone (11, 50),

$$\kappa^{\alpha\beta} = \frac{1}{k_B T^2 \Omega N} \sum_\lambda n_\lambda (n_\lambda + 1) (\hbar \omega_\lambda)^2 v_\lambda^\alpha F_\lambda^\beta \quad (\text{E15})$$

where \hbar is the Plank constant over 2π , Ω is the volume of unit cell. Here, the first Brillouin zone is discretized by a $28 \times 28 \times 28$ \mathbf{q} mesh. v_λ^α is the group velocity of phonon mode λ along direction α , which can be calculated from phonon dispersion relation,

$$v_\lambda^\alpha = \frac{\partial \omega}{\partial q^\alpha} \quad (\text{E16})$$

where q^α is the wave vector along direction α .

We calculated the second and third order interatomic force constants (IFCs). Second-order IFCs are required for deriving phonon dispersion relation. We obtained second-order IFCs based on density functional theory (DFT) (51, 52) and density functional perturbation theory (DFPT) (53) using Quantum ESPRESSO (54, 55) package respectively. In self-consistent calculations of electronic structure using plane-wave basis, we used norm-conserving pseudopotentials under local density approximation for both boron and arsenic (56). The kinetic energy cutoff for electronic wavefunctions was set as 80 Ry. The lattice constant of BAs is determined by minimizing the total energy of the system in ground-state. After self-consistent calculations of electronic structure, DFPT was applied to obtain the second-order IFCs. For both DFT and DFPT calculations, we used $6 \times 6 \times 6$ Monkhorst-Pack k-points meshes. Third-order IFCs are required for three phonon process of the intrinsic phonon-phonon scattering. The third-

order IFCs were obtained from a $4 \times 4 \times 4$ supercell with 128 atoms, using finite displacement method in real space. Up to fifth nearest neighbors were considered. A package `thirdorder.py` (57) was used to generate an irreducible set of displacements and then extract third order IFCs from the forces acting on atoms under each displacements. The forces acting on atoms was calculated by DFT. After obtaining the IFCs, the lattice thermal conductivity was computed using ShengBTE package (50, 58).

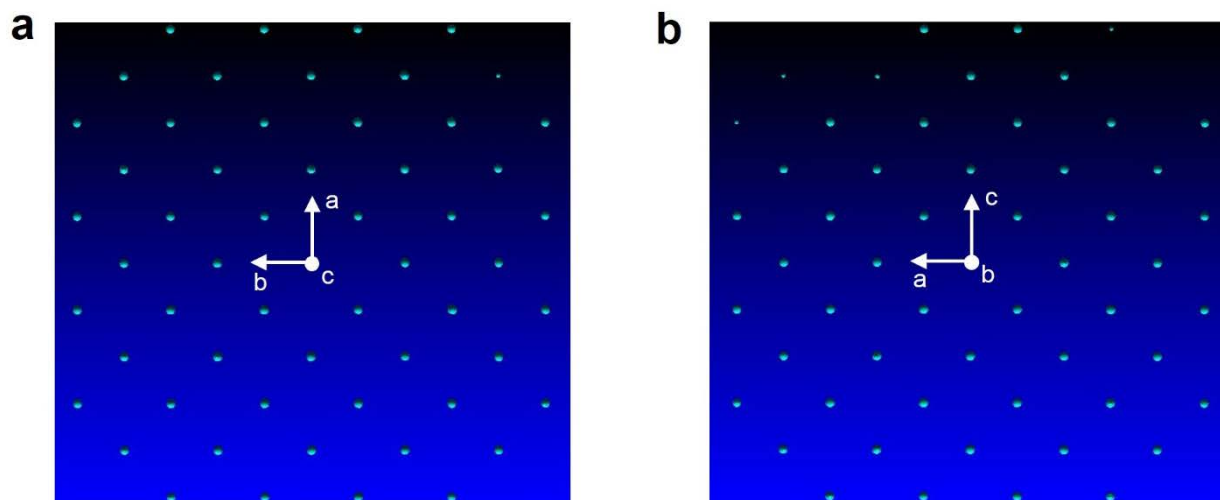


Figure S1. Verification of the crystal quality of BAs. The reciprocal lattice of the BAs crystal sample measured from the single-crystal X-ray data for the (001) plane (**a**), (010) plane (**b**), and (100) plane (Figure 1F in the main text), validates that the entire BAs crystal sample is a single-crystal domain without any impurities or lattice twinning.

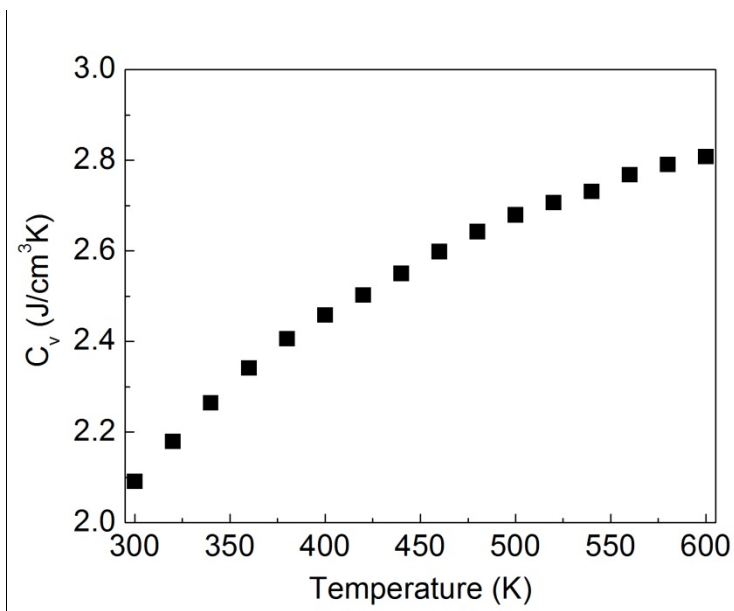


Figure S2. Temperature-dependent volumetric heat capacity of BAs.

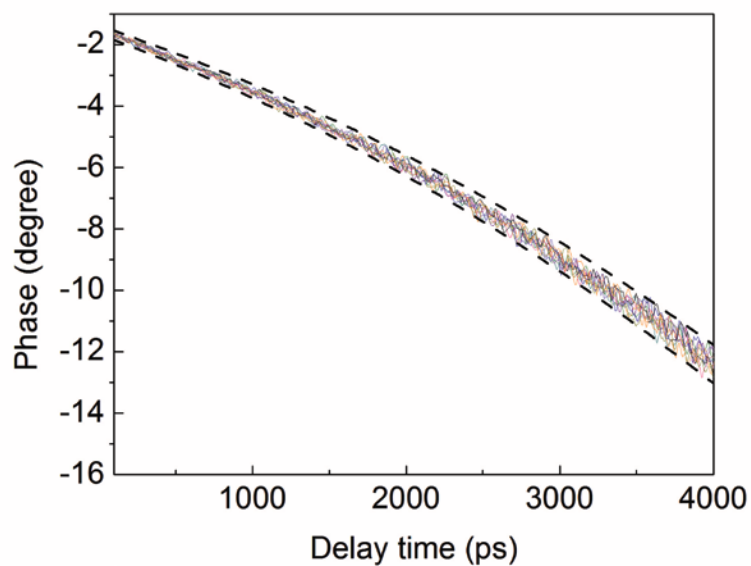


Figure S3. Ten representative TDTR measurement curves (color lines) are shown. The black dashed curves are calculated using the thermal conductivity changed by $\pm 10\%$.

References and Notes

1. M. M. Waldrop, The chips are down for Moore's law. *Nature* **530**, 144–147 (2016). [doi:10.1038/530144a](https://doi.org/10.1038/530144a) [Medline](#)
2. P. Ball, Computer engineering: Feeling the heat. *Nature* **492**, 174–176 (2012). [doi:10.1038/492174a](https://doi.org/10.1038/492174a) [Medline](#)
3. S. Chu, A. Majumdar, Opportunities and challenges for a sustainable energy future. *Nature* **488**, 294–303 (2012). [doi:10.1038/nature11475](https://doi.org/10.1038/nature11475) [Medline](#)
4. W. L. Arman Shehabi, Sarah Smith, Dale Sartor, Richard Brown, Magnus Herrlin, Jonathan Koomey, Eric Masanet, Nathaniel Horner, Inês Azevedo, United States Data Center Energy Usage Report (2016); <https://ses.lbl.gov/publications/united-states-data-center-energy>.
5. International Technology Roadmap for Semiconductors, ITRS 2.0 2015 Edition; www.itrs2.net/.
6. J. M. Ziman, *Electrons and Phonons: The Theory of Transport Phenomena in Solids*. Oxford Classic Texts in the Physical Sciences (1960).
7. G. A. Slack, Nonmetallic crystal with high thermal conductivity. *J. Phys. Chem. Solids* **34**, 321–335 (1973). [doi:10.1016/0022-3697\(73\)90092-9](https://doi.org/10.1016/0022-3697(73)90092-9)
8. L. Lindsay, D. A. Broido, T. L. Reinecke, First-principles determination of ultrahigh thermal conductivity of boron arsenide: A competitor for diamond? *Phys. Rev. Lett.* **111**, 025901 (2013). [doi:10.1103/PhysRevLett.111.025901](https://doi.org/10.1103/PhysRevLett.111.025901) [Medline](#)
9. N. Mingo, D. A. Broido, Lattice thermal conductivity crossovers in semiconductor nanowires. *Phys. Rev. Lett.* **93**, 246106 (2004). [doi:10.1103/PhysRevLett.93.246106](https://doi.org/10.1103/PhysRevLett.93.246106) [Medline](#)
10. N. Mingo, D. A. Broido, Carbon nanotube ballistic thermal conductance and its limits. *Phys. Rev. Lett.* **95**, 096105 (2005). [doi:10.1103/PhysRevLett.95.096105](https://doi.org/10.1103/PhysRevLett.95.096105) [Medline](#)
11. A. Ward, D. A. Broido, D. A. Stewart, G. Deinzer, Ab initio theory of the lattice thermal conductivity in diamond. *Phys. Rev. B* **80**, 125203 (2009). [doi:10.1103/PhysRevB.80.125203](https://doi.org/10.1103/PhysRevB.80.125203)
12. K. Esfarjani, G. Chen, H. T. Stokes, Heat transport in silicon from first-principles calculations. *Phys. Rev. B* **84**, 85204 (2011). [doi:10.1103/PhysRevB.84.085204](https://doi.org/10.1103/PhysRevB.84.085204)
13. L. Lindsay, D. A. Broido, T. L. Reinecke, Thermal conductivity and large isotope effect in GaN from first principles. *Phys. Rev. Lett.* **109**, 095901 (2012). [doi:10.1103/PhysRevLett.109.095901](https://doi.org/10.1103/PhysRevLett.109.095901) [Medline](#)
14. M. N. Luckyanova, J. Garg, K. Esfarjani, A. Jandl, M. T. Bulsara, A. J. Schmidt, A. J. Minnich, S. Chen, M. S. Dresselhaus, Z. Ren, E. A. Fitzgerald, G. Chen, Coherent phonon heat conduction in superlattices. *Science* **338**, 936–939 (2012). [doi:10.1126/science.1225549](https://doi.org/10.1126/science.1225549) [Medline](#)
15. Y. Hu, L. Zeng, A. J. Minnich, M. S. Dresselhaus, G. Chen, Spectral mapping of thermal conductivity through nanoscale ballistic transport. *Nat. Nanotechnol.* **10**, 701–706 (2015). [doi:10.1038/nnano.2015.109](https://doi.org/10.1038/nnano.2015.109) [Medline](#)

16. T. Feng, L. Lindsay, X. Ruan, Four-phonon scattering significantly reduces intrinsic thermal conductivity of solids. *Phys. Rev. B* **96**, 161201 (2017).
[doi:10.1103/PhysRevB.96.161201](https://doi.org/10.1103/PhysRevB.96.161201)
17. C. Uher, Keeping it cool. *Physics (College Park Md.)* **6**, 76 (2013). [doi:10.1103/Physics.6.76](https://doi.org/10.1103/Physics.6.76)
18. D. A. Broido, L. Lindsay, T. L. Reinecke, *Ab initio* study of the unusual thermal transport properties of boron arsenide and related materials. *Phys. Rev. B* **88**, 214303 (2013).
[doi:10.1103/PhysRevB.88.214303](https://doi.org/10.1103/PhysRevB.88.214303)
19. R. M. Wentzcovitch, M. L. Cohen, P. K. Lam, Theoretical study of BN, BP, and BAs at high pressures. *Phys. Rev. B Condens. Matter* **36**, 6058–6068 (1987).
[doi:10.1103/PhysRevB.36.6058](https://doi.org/10.1103/PhysRevB.36.6058) [Medline](#)
20. M. Lax, P. Hu, V. Narayanamurti, Spontaneous phonon decay selection rule: N and U processes. *Phys. Rev. B* **23**, 3095–3097 (1981). [doi:10.1103/PhysRevB.23.3095](https://doi.org/10.1103/PhysRevB.23.3095)
21. L. Lindsay, D. A. Broido, T. L. Reinecke, Phonon-isotope scattering and thermal conductivity in materials with a large isotope effect: A first-principles study. *Phys. Rev. B* **88**, 144306 (2013). [doi:10.1103/PhysRevB.88.144306](https://doi.org/10.1103/PhysRevB.88.144306)
22. S. Tamura, Isotope scattering of large-wave-vector phonons in GaAs and InSb: Deformation-dipole and overlap-shell models. *Phys. Rev. B* **30**, 849–854 (1984).
[doi:10.1103/PhysRevB.30.849](https://doi.org/10.1103/PhysRevB.30.849)
23. J. A. Perri, S. Laplaca, B. Post, New group III–group V Compounds: BP and BAs. *Acta Crystallogr.* **11**, 310 (1958). [doi:10.1107/S0365110X58000827](https://doi.org/10.1107/S0365110X58000827)
24. F. V. Williams, R. A. Ruehrwein, The preparation and properties of boron phosphides and arsenides. *J. Am. Chem. Soc.* **82**, 1330–1332 (1960). [doi:10.1021/ja01491a014](https://doi.org/10.1021/ja01491a014)
25. J. Osugi, K. Shimizu, Y. Tanaka, Chemical reaction at high temperature and high pressure. II Reaction of boron and arsenic at high temperature and high pressure. *Proc. Jpn. Acad.* **42**, 48 (1966).
26. S. M. Ku, Preparation and properties of boron arsenides and boron arsenide-gallium arsenide mixed crystals. *J. Electrochem. Soc.* **113**, 813 (1966). [doi:10.1149/1.2424125](https://doi.org/10.1149/1.2424125)
27. A. F. Armington, Vapor transport of boron, boron phosphide and boron arsenide. *J. Cryst. Growth* **1**, 47–48 (1967). [doi:10.1016/0022-0248\(67\)90007-3](https://doi.org/10.1016/0022-0248(67)90007-3)
28. T. L. Chu, A. E. Hyslop, Crystal growth and properties of boron monoarsenide. *J. Appl. Phys.* **43**, 276–279 (1972). [doi:10.1063/1.1661106](https://doi.org/10.1063/1.1661106)
29. P. Rudolph, Ed., *Handbook of Crystal Growth, Vol. II, Bulk Crystal Growth* (Elsevier, 2015); <http://store.elsevier.com/Handbook-of-Crystal-Growth/isbn-9780444633033/>.
30. B. Lv, Y. Lan, X. Wang, Q. Zhang, Y. Hu, A. J. Jacobson, D. Broido, G. Chen, Z. Ren, C.-W. Chu, Experimental study of the proposed super-thermal-conductor: BAs. *Appl. Phys. Lett.* **106**, 074105 (2015). [doi:10.1063/1.4913441](https://doi.org/10.1063/1.4913441)
31. F. Tian, B. Song, B. Lv, J. Sun, S. Huyan, Q. Wu, J. Mao, Y. Ni, Z. Ding, S. Huberman, T.-H. Liu, G. Chen, S. Chen, C.-W. Chu, Z. Ren, Seeded growth of boron arsenide single

- crystals with high thermal conductivity. *Appl. Phys. Lett.* **112**, 031903 (2018).
[doi:10.1063/1.5004200](https://doi.org/10.1063/1.5004200)
32. N. H. Protik, J. Carrete, N. A. Katcho, N. Mingo, D. Broido, Ab initio study of the effect of vacancies on the thermal conductivity of boron arsenide. *Phys. Rev. B* **94**, 045207 (2016).
[doi:10.1103/PhysRevB.94.045207](https://doi.org/10.1103/PhysRevB.94.045207)
33. B. E. Warren, *X-ray Diffraction* (Addison-Wesley, MA, 1969).
34. Materials and methods are available as supplementary materials.
35. D. B. Williams, C. B. Carter, *Transmission Electron Microscopy: A Textbook for Materials Science* (Springer, Boston, MA, 2009).
36. J. S. Kang, H. Wu, Y. Hu, Thermal properties and phonon spectral characterization of synthetic boron phosphide for high thermal conductivity applications. *Nano Lett.* **17**, 7507–7514 (2017). [doi:10.1021/acs.nanolett.7b03437](https://doi.org/10.1021/acs.nanolett.7b03437) [Medline](#)
37. D. G. Onn, A. Witek, Y. Z. Qiu, T. R. Anthony, W. F. Banholzer, Some aspects of the thermal conductivity of isotopically enriched diamond single crystals. *Phys. Rev. Lett.* **68**, 2806–2809 (1992). [doi:10.1103/PhysRevLett.68.2806](https://doi.org/10.1103/PhysRevLett.68.2806) [Medline](#)
38. L. Wei, P. K. Kuo, R. L. Thomas, T. R. Anthony, W. F. Banholzer, Thermal conductivity of isotopically modified single crystal diamond. *Phys. Rev. Lett.* **70**, 3764–3767 (1993).
[doi:10.1103/PhysRevLett.70.3764](https://doi.org/10.1103/PhysRevLett.70.3764) [Medline](#)
39. J. R. Olson, R. O. Pohl, J. W. Vandersande, A. Zoltan, T. R. Anthony, W. F. Banholzer, Thermal conductivity of diamond between 170 and 1200 K and the isotope effect. *Phys. Rev. B Condens. Matter* **47**, 14850–14856 (1993). [doi:10.1103/PhysRevB.47.14850](https://doi.org/10.1103/PhysRevB.47.14850) [Medline](#)
40. A. Maradudin, A. Fein, Scattering of neutrons by an anharmonic crystal. *Phys. Rev.* **128**, 2589–2608 (1962). [doi:10.1103/PhysRev.128.2589](https://doi.org/10.1103/PhysRev.128.2589)
41. L. Lindsay, D. A. Broido, Three-phonon phase space and lattice thermal conductivity in semiconductors. *J. Phys. Condens. Matter* **20**, 165209 (2008). [doi:10.1088/0953-8984/20/16/165209](https://doi.org/10.1088/0953-8984/20/16/165209)
42. F. Yang, C. Dames, Mean free path spectra as a tool to understand thermal conductivity in bulk and nanostructures. *Phys. Rev. B* **87**, 035437 (2013).
[doi:10.1103/PhysRevB.87.035437](https://doi.org/10.1103/PhysRevB.87.035437)
43. G. T. Hohensee, R. B. Wilson, D. G. Cahill, Thermal conductance of metal-diamond interfaces at high pressure. *Nat. Commun.* **6**, 6578 (2015). [doi:10.1038/ncomms7578](https://doi.org/10.1038/ncomms7578) [Medline](#)
44. A. Sood, J. Cho, K. D. Hobart, T. I. Feygelson, B. B. Pate, M. Asheghi, D. G. Cahill, K. E. Goodson, Anisotropic and inhomogeneous thermal conduction in suspended thin-film polycrystalline diamond. *J. Appl. Phys.* **119**, 175103 (2016). [doi:10.1063/1.4948335](https://doi.org/10.1063/1.4948335)
45. J. P. Feser, D. G. Cahill, Probing anisotropic heat transport using time-domain thermoreflectance with offset laser spots. *Rev. Sci. Instrum.* **83**, 104901 (2012).
[doi:10.1063/1.4757863](https://doi.org/10.1063/1.4757863) [Medline](#)

46. A. J. Schmidt, X. Chen, G. Chen, Pulse accumulation, radial heat conduction, and anisotropic thermal conductivity in pump-probe transient thermoreflectance. *Rev. Sci. Instrum.* **79**, 114902 (2008). [doi:10.1063/1.3006335](https://doi.org/10.1063/1.3006335) [Medline](#)
47. D. G. Cahill, Analysis of heat flow in layered structures for time-domain thermoreflectance. *Rev. Sci. Instrum.* **75**, 5119–5122 (2004). [doi:10.1063/1.1819431](https://doi.org/10.1063/1.1819431)
48. A. Ektarawong, S. I. Simak, B. Alling, First-principles prediction of stabilities and instabilities of compounds and alloys in the ternary B-As-P system. *Phys. Rev. B* **96**, 024202 (2017). [doi:10.1103/PhysRevB.96.024202](https://doi.org/10.1103/PhysRevB.96.024202)
49. S. Tamura, Isotope scattering of dispersive phonons in Ge. *Phys. Rev. B* **27**, 858–866 (1983). [doi:10.1103/PhysRevB.27.858](https://doi.org/10.1103/PhysRevB.27.858)
50. W. Li, J. Carrete, N. A. Katcho, N. Mingo, B. T. E. Sheng, A solver of the Boltzmann transport equation for phonons. *Comput. Phys. Commun.* **185**, 1747–1758 (2014). [doi:10.1016/j.cpc.2014.02.015](https://doi.org/10.1016/j.cpc.2014.02.015)
51. P. Hohenberg, W. Kohn, Inhomogeneous electron gas. *Phys. Rev.* **136** (3B), B864–B871 (1964). [doi:10.1103/PhysRev.136.B864](https://doi.org/10.1103/PhysRev.136.B864)
52. W. Kohn, L. J. Sham, Self-consistent equations including exchange and correlation effects. *Phys. Rev.* **140** (4A), A1133–A1138 (1965). [doi:10.1103/PhysRev.140.A1133](https://doi.org/10.1103/PhysRev.140.A1133)
53. S. Baroni, S. de Gironcoli, A. Dal Corso, P. Giannozzi, Phonons and related crystal properties from density-functional perturbation theory. *Rev. Mod. Phys.* **73**, 515–562 (2001). [doi:10.1103/RevModPhys.73.515](https://doi.org/10.1103/RevModPhys.73.515)
54. P. Giannozzi, S. Baroni, N. Bonini, M. Calandra, R. Car, C. Cavazzoni, D. Ceresoli, G. L. Chiarotti, M. Cococcioni, I. Dabo, A. Dal Corso, S. de Gironcoli, S. Fabris, G. Fratesi, R. Gebauer, U. Gerstmann, C. Gougoussis, A. Kokalj, M. Lazzeri, L. Martin-Samos, N. Marzari, F. Mauri, R. Mazzarello, S. Paolini, A. Pasquarello, L. Paulatto, C. Sbraccia, S. Scandolo, G. Sclauzero, A. P. Seitsonen, A. Smogunov, P. Umari, R. M. Wentzcovitch, QUANTUM ESPRESSO: A modular and open-source software project for quantum simulations of materials. *J. Phys. Condens. Matter* **21**, 395502 (2009). [doi:10.1088/0953-8984/21/39/395502](https://doi.org/10.1088/0953-8984/21/39/395502) [Medline](#)
55. P. Giannozzi, O. Andreussi, T. Brumme, O. Bunau, M. Buongiorno Nardelli, M. Calandra, R. Car, C. Cavazzoni, D. Ceresoli, M. Cococcioni, N. Colonna, I. Carnimeo, A. Dal Corso, S. de Gironcoli, P. Delugas, R. A. DiStasio Jr., A. Ferretti, A. Floris, G. Fratesi, G. Fugallo, R. Gebauer, U. Gerstmann, F. Giustino, T. Gorni, J. Jia, M. Kawamura, H.-Y. Ko, A. Kokalj, E. Küçükbenli, M. Lazzeri, M. Marsili, N. Marzari, F. Mauri, N. L. Nguyen, H.-V. Nguyen, A. Otero-de-la-Roza, L. Paulatto, S. Poncé, D. Rocca, R. Sabatini, B. Santra, M. Schlipf, A. P. Seitsonen, A. Smogunov, I. Timrov, T. Thonhauser, P. Umari, N. Vast, X. Wu, S. Baroni, Advanced capabilities for materials modelling with Quantum ESPRESSO. *J. Phys. Condens. Matter* **29**, 465901 (2017). [doi:10.1088/1361-648X/aa8f79](https://doi.org/10.1088/1361-648X/aa8f79) [Medline](#)
56. We used the pseudopotentials B.pz-n-kjpaw_psl.0.1.UPF and As.pz-n-kjpaw_psl.0.2.UPF from the Quantum ESPRESSO pseudopotential data base: <http://www.quantum-espresso.org/pseudopotentials>.

57. W. Li, L. Lindsay, D. A. Broido, D. A. Stewart, N. Mingo, Thermal conductivity of bulk and nanowire $\text{Mg}_2\text{Si}_x\text{Sn}_{1-x}$ alloys from first principles. *Phys. Rev. B* **86**, 174307 (2012).
[doi:10.1103/PhysRevB.86.174307](https://doi.org/10.1103/PhysRevB.86.174307)
58. W. Li, N. Mingo, L. Lindsay, D. A. Broido, D. A. Stewart, N. A. Katcho, Thermal conductivity of diamond nanowires from first principles. *Phys. Rev. B* **85**, 195436 (2012).
[doi:10.1103/PhysRevB.85.195436](https://doi.org/10.1103/PhysRevB.85.195436)